Journal of Aerosol Science 167 (2023) 106100

Contents lists available at ScienceDirect

Journal of Aerosol Science

journal homepage: www.elsevier.com/locate/jaerosci

Retrieval of refractive indices of ten volcanic ash samples in the infrared, visible and ultraviolet spectral region

Alexandre Deguine [a,b,*], Denis Petitprez [b], Lieven Clarisse [c], Lise Deschutter [a,b], Karen Fontijn [d], Hervé Herbin [a]

[a] Univ. Lille, CNRS, UMR 8518 – LOA – Laboratoire d'Optique Atmosphérique, F-59000 Lille, France
[b] Univ. Lille, CNRS, UMR 8522 – PC2A – Laboratoire de Physicochimie des Processus de Combustion et de l'Atmosphère, F-59000 Lille, France
[c] Université libre de Bruxelles (ULB), Spectroscopy, Quantum Chemistry and Atmospheric Remote Sensing (SQUARES), Brussels, Belgium
[d] Université libre de Bruxelles (ULB), ,Laboratoire G-Time, Department of Geosciences, Environment and Society, Brussels, Belgium

ARTICLE INFO

Editor: Dr. Chris Hogan

Keywords:
Volcanic ash
Complex refractive index
Infrared
Ultraviolet
Spectroscopy
Chemical composition
Aerosols

ABSTRACT

Volcanic eruptions can emit large amounts of ash into the atmosphere, which can have significant impacts on infrastructure, human health, agriculture and air traffic. Remote sensing instruments can efficiently detect airborne ash plumes, and the measured spectra can be exploited to obtain information on the physical characteristics of ash (grain size distribution, concentration, optical depth). The key parameter on which all such satellite retrievals depend is the complex refractive index (CRI) which remains one of the largest sources of uncertainty in the retrieval process. Here we present a complementary dataset of refractive indices of volcanic ash to that published by Deguine et al. (2020), to cover a part of the major explosive eruptions occurred during the past 50 years. These CRIs were obtained using an innovative experimental methodology which consists in measuring simultaneously the extinction spectra in the IR and UV/visible domain and the size distribution of ash in suspension in a nitrogen flow. These experimental data are the main input to the retrieval process of CRI. The numerical routine uses Mie theory coupled with Kramers–Kronig relationship to retrieve the imaginary and the real part of the complex refractive index. This methodology has been successfully applied on samples collected from various eruptions and deposits in Indonesia (Kelud), Chile (Chaitén), Italy (Stromboli), Russia (Karymsky), Tanzania (Rungwe, Mount Meru), Ethiopia (Corbetti), Philippines (Taal, Pinatubo) and USA (Mount St. Helens). Significant variations of the real and imaginary part of the CRI are observed according to the chemical composition of the samples. Moreover, the sensitivity of the CRI to chemical composition and mineralogical structure (amorphous/crystalline fraction) has been investigated and shows a strong dependence of the CRI on these parameters.

1. Introduction

During an explosive volcanic eruption, a large amount of particles are ejected into the atmosphere, ranging from very fine particles (<1 μm) to coarse particles of several centimetres or even more, and collectively called "tephra". The term "volcanic ash" refers to small particles of rock (less than 2 mm) dispersed into the atmosphere. In the case of highly explosive eruptions, volcanic ash can be propelled up to tens of kilometres of altitude (Kaminski et al., 2011) and even higher for recent eruptions such as the

* Corresponding author at: Univ. Lille, CNRS, UMR 8518 – LOA – Laboratoire d'Optique Atmosphérique, F-59000 Lille, France.
E-mail address: alexandre.deguine@univ-lille.fr (A. Deguine).

https://doi.org/10.1016/j.jaerosci.2022.106100
Received 22 July 2022; Received in revised form 12 October 2022; Accepted 4 November 2022
Available online 10 November 2022

Hunga Tonga volcano with particles injected at 55 km height (Carr, Horváth, Wu, & Friberg, 2022). The average particle size in a volcanic ash plume decreases over time due to sedimentation of larger particles. These large particles (>100 μm) fall down quickly near their sources and can have a significant impact on human health and agriculture (Baxter & Horwell, 2015; Wilson et al., 2012). Particles greater than tens of microns have a residence time in the atmosphere of a few hours. The finest particles, ranging from a few microns to tens of microns, can persist in the atmosphere for several days (Gouhier et al., 2019; Rossi, Bagheri, Beckett, & Bonadonna, 2021), with an impact on the interaction between solar radiation and the atmosphere.

Ash clouds drift in relation to tropospheric or stratospheric winds and can be transported over very long distances away from their sources. At local scale, the coarse fraction of volcanic ash particles are deposited on building and plantations causing important damages on structures and local food supply (Thompson, Lindsay, Wilson, Biass, & Sandri, 2016; Wilson & Cole, 2007). The fine fraction of aerosols has a direct impact on the human health by causing lungs diseases when a large amount of volcanic ash aerosols are inhaled and also when the exposure time is high (including chronic exposure) (Horwell & Baxter, 2006; Lombardo et al., 2013; Mueller, Cowie, Horwell, Hurley, & Baxter, 2020; Tomašek et al., 2021). At global scale, ash clouds likely to be encountered by aircraft are made up of the finest particles (<1 μm). At night, ash clouds are not visible to pilots, and do not appear differently from meteorological clouds on radar. Even during the day, ash clouds may not be identified due to their mixing with water vapour or too little colouration. The concentration of ash as a function of distance depends on the height of the ash column, weather conditions (wind speed, shear as a function of altitude, especially for stratospheric winds) and changes in temperature. Volcanic ash, due to its abrasive nature and its difficulty in being detected by radar on aircraft board, makes it a major threat to aviation (Casadevall, Delos Reyes, & Schneider, 1996; Dean, Taltavull, & Clyne, 2016; Guffanti, Casadevall, & Budding, 2010; Shinozaki, Roberts, van de Goor, & Clyne, 2013). In the past, volcanic ash has caused extensive physical damage to aircraft, with economic costs well in excess of $250 million between 1982 and 2000 (Support to Aviation Control Service data). In addition, the economic costs to airlines, due to flight cancellations, delays, compensation to passengers etc., can be high as demonstrated by the consequences of the eruption of the Icelandic volcano Eyjafjallajökull in 2010 (Ansmann et al., 2010; Donovan & Oppenheimer, 2010; Gudmundsson, Pedersen, Vogfjörd, Thorbjarnardóttir, Jakobsdóttir, & Roberts, 2010; Sigmundsson & Höskuldsson, 2010), with estimates of 1 billion dollars. By absorbing terrestrial radiation and scattering the solar radiation, volcanic ashes also have a significant influence on the Earth's radiation balance (Laakso et al., 2016; Zhu et al., 2020)

The properties of ash clouds such as plume height, concentration and particle size distribution are studied by ground-based and satellite remote sensing techniques. The prediction of ash cloud trajectories has required the development of transport and dispersion models of in-situ volcanic ash that can calculate the trajectory of an ash cloud at the scale of a continent or the hemisphere (Cao, Bursik, Yang, & Patra, 2021; Harvey et al., 2018; Heffter & Stunder, 1993; Peterson et al., 2015). Volcanological parameters such as plume height, eruptive rate, duration of eruption, ash distribution with altitude and particle size distribution are essential in real time during an event to constrain these models, often with limited observations (de Michele et al., 2019; Stohl et al., 2011). Improved prediction of ash cloud trajectories and fallout is a major issue in order to better assess threats to aviation, public health and air quality. For this, it seems essential to improve our knowledge of the optical and physico-chemical properties of volcanic ash. Numerous studies have focused on the study of these optical properties highlighting the need to determine the complex refractive index (CRI), the key parameter from which all these quantities (aerosol optical thickness, single scattering albedo, height of the plume, mass loading, particle radius) are calculated to characterize all the optical properties (Deguine et al., 2020; Herbin, Pujol, Hubert, & Petitprez, 2017; Hubert, Herbin, Visez, Pujol, & Petitprez, 2017; Reed, Peters, McPheat, & Grainger, 2018). The oldest approach implemented by Pollack, Toon, and Khare (1973) is based on the determination of CRIs of bulk materials such as basalt, andesite and rhyolite that represent common magmatic rock compositions erupted from volcanoes. However, the measurement of CRI on bulk materials, as well as on pellets suffers from many limitations such as: minimization of the scattering effect, the lack of knowledge of the size of the particles making up the sample in a pellet, or the modification of the morphology of the particles during the pellet building inducing a modification of the vibrational properties of molecules.

In order to make the measurements more representative for real atmospheric conditions, several studies have highlighted the need to determine the CRIs of volcanic ash for suspended particles. These different studies show a drastically different behaviour of the indices compared to those proposed by the methods using pellets and on bulk material (Egan, Hilgeman, & Pang, 1975; Pollack et al., 1973; Volz, 1973). The determination of new refractive indices aims to better approach the real conditions of transport of volcanic ash in the atmosphere and thus to be able to reproduce the spectra of extinctions recorded by atmospheric sounders such as the Infrared Atmospheric Sounding Interferometer (IASI). As pointed out by Clarisse et al. (2010), infrared sounders are not able to reproduce the spectra observed with the ash indices from the literature. In this study, we determine complex refractive indices for different volcanic ash samples in the field of UV/visible and infrared (IR). The determination of the CRIs is based on the methodology described in Deguine et al. (2020). This article consists of an extension of the latter, with the determination of a wide range of samples with various chemical and mineralogical compositions covering almost the entire Total Alkali–Silica (TAS) diagram (see Fig. 1). Moreover, these complementary data will help to feed existing databases such as GEISA (https://geisa.aeris-data.fr), HITRAN (https://hitran.org) and ARIA (http://eodg.atm.ox.ac.uk), which still contains very few modern CRI measurements and which remains the main source for modellers when simulating the transport of ashes in the atmosphere (Cai et al., 2018; Mosaffaei & Jahani, 2020; Plu et al., 2021).

This article is divided into four main sections. The first section describes the samples taken from the different sources. The second section refers to the experimental laboratory measurements necessary for the extraction of CRIs and the numerical approach used to retrieve refractive indices. The third section presents the extinction spectra recorded in the laboratory with retrieved ones from numerical simulations and the CRIs obtained using the optimal estimation method. The last section discusses the comparison of four datasets of refractive index from ash with a close chemical and mineralogical composition and analyses the impact of amorphous/crystalline fraction on CRIs.

Table 1
The volcanic ash samples and their major elemental composition determined by an XRF analysis (in oxide weight %). Note that analyses are on dried/ignited powders.

Volcano Eruption date	Type	SiO_2	Al_2O_3	Na_2O	K_2O	Fe_2O_3	CaO	MgO	TiO_2	Amorphous fraction (%)
Mount St. Helens May 1980	Dacite	66.8	16.0	4.9	1.9	3.9	4.3	1.1	0.6	46.0
Stromboli March 2019	Trachy-Basalt	49.5	20.3	3.0	2.9	8.2	10.7	2.5	1.1	27.6
Pinatubo June 1991	Dacite	64.8	16.3	4.7	1.9	3.4	5.6	1.8	0.4	19.9
Kelud February 2014	Andesite	58.8	17.9	3.8	1.2	6.6	8.9	1.3	0.7	31.6
Karymsky March 2014	Trachy-Andesit	61.5	16.9	4.9	1.8	6.3	6.0	1.0	1.0	40.7
Corbetti 2017	Rhyolite	74.0	9.8	5.6	4.7	4.8	0.2	0.1	0.3	94.5
Meru MXP3	Phonolite	53.7	21.8	8.3	5.7	5.2	2.7	0.4	0.9	86.7
Taal 1977	Basaltic-Andesite	54.3	16.1	3.2	2.0	12.1	7.4	2.5	1.2	47.8
Rungwe Isongole Pumice eruption	Trachydacite	62.1	19.0	6.0	6.7	3.2	1.0	0.4	0.8	89.7
Chaitén February 2009	Rhyolite	73.0	14.8	4.5	3.3	1.7	1.8	0.4	0.2	34.5

2. Origin and selection of samples

New volcanic ash samples have been chosen to be complementary in terms of chemical composition, to the samples already measured in Deguine et al. (2020). These samples cover a wide range of chemical compositions and represent an important part of wide range of igneous rocks composing volcanoes. Table 1 lists all the samples selected in this study and reports their chemical compositions obtained by a semi-quantitative X-ray fluorescence (XRF) analysis using a S4 Pioneer Bruker. The XRF technique was done in the Service Materials engineering, Characterization, Synthesis and Recycling (4MAT) of the Université libre de Bruxelles (ULB) and samples were deposited on a boric acid pellet and compressed at 8 tons. This chemical analysis provides the oxide composition of the samples within 2%–3% of error on the major component (SiO_2 in the case of volcanic ash) (Remya Devi et al., 2015).

Fig. 1 represents the TAS diagram and shows the high diversity of the bulk chemical composition of the samples used in this study. The main interest is to cover as wide as possible the full diagram to represent as many volcanoes as possible. In this study, a total of ten volcanic ash samples from tephra fall deposits spanning a range of chemical compositions were selected: a medium-K basaltic andesite from an 18th century eruption at the Main Crater Taal volcano (Philippines; Delos Reyes et al., 2018), a phonolite from the MXP3 deposit of Mt Meru (Tanzania; Kisaka et al., 2021), a trachyte from the Isongole Pumice deposit of Rungwe volcano (Tanzania; Fontijn et al., 2010) and a peralkaline rhyolite from a Late-Holocene eruption at Corbetti volcano (Ethiopia; Fontijn et al., 2018). These samples were deliberately selected to cover a range of compositions, especially alkaline, to be representative for eruptions in East Africa, and which are known to be potentially highly explosive (Fontijn et al., 2010, 2018; Kisaka et al., 2021). Samples of the historical eruptions of Pinatubo in 1991 and Mount Saint Helens has been also chosen due to their large impact on the climate in twentieth century. Moreover, a high silicate sample from Chile (Chaitén) was selected to compare to the previous CRIs obtained from Deguine et al. (2020). To cover a large spatial region, we decided to analyse samples from Indonesia (Kelud), from Russia (Karymsky) and from Italy (Stromboli). All these volcanoes are known to commonly erupt or had a really strong explosive eruption in the recent past that was analysed by spatial remote sensing (Vernier et al., 2016). The combination of the samples measured in Deguine et al. (2020) with those in this study, are covering an important part of the major eruptions of the 20th century.

3. Experimental and numerical approach

The setup used in this study as well as the numerical procedure for data retrieval has already been described in several previous papers (see Deguine et al., 2020; Herbin et al., 2017; Hubert et al., 2017). A brief summary will be given in this section.

3.1. Laboratory measurements

First, volcanic ash particles are dispersed using a flow of nitrogen (2 $L.min^{-1}$) combined with a mechanical agitation (rotation of a magnetic stirrer). Then, the ash flows through a buffer volume to create an homogeneous cloud of aerosols. Afterwards, the

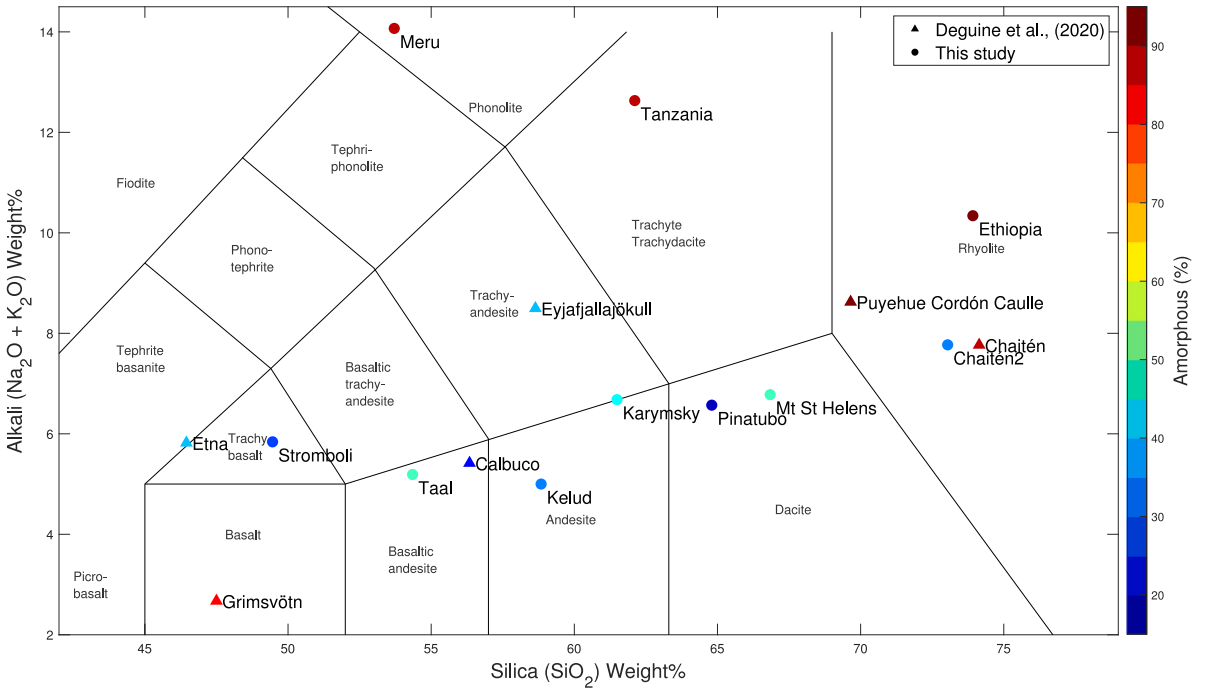

Fig. 1. TAS diagram (Bas, Maitre, Streckeisen, & Zanettin, 1986) with the ash samples measured in this study, and those of previous study from Deguine et al. 2020. The colour scale gives the proportion of amorphous matter in the samples determined by X-ray diffraction (XRD). (For interpretation of the references to colour in this figure legend, the reader is referred to the web version of this article.)

extinction spectra is recorded from 690 to 3600 cm^{-1} using a IS50 (Thermo Scientific) Fourier transform infrared spectrometer. This spectrometer is composed of a multi-pass cell (White cell) with an optical length of 10 meters and horizontally oriented to minimized the deposition of particles on the mirrors. Moreover, to overcome the significant absorption of water vapour and carbon dioxide (CO_2) in the spectral range of the IR, a purge is set up. This is achieved by a continuous flow of nitrogen (N_2) injected in the interferometer and, for several hours before the experiment, in the cell. For the UV-visible part, the spectrometer records the extinction spectra from 10 000 to 32 500 cm^{-1}. An aerodynamic particle sizer is used (TSI- APS3321) to measure the aerodynamic diameter of the particles between 0.523 and 20 μm, with a resolution of 32 channels per decade (52 channels in total). Nevertheless, to estimate the complex refractive index of ash, the retrieval procedure needs to know the geometric diameter which can be calculated using equation 1 in continuum regime conditions (DeCarlo, Slowik, Worsnop, Davidovits, & Jimenez, 2004):

$$2r_g = 2r_a\sqrt{\frac{\chi\rho_0}{\rho}} \tag{1}$$

with ρ_0 the standard density (1 $g.cm^{-3}$) and ρ the particle density in $g.cm^{-3}$. r_a and r_g are the aerodynamic and geometric radius of the particles and χ the dynamic shape factor. Therefore, the density and the dynamic shape factor have to be estimated. In that way, the particle densities were determined from the density of oxides (Railsback, 2006), weighted with their fractional abundance, as measured by the XRF analysis. The dynamic shape factors χ can be estimated by using microscopic analysis such as SEM (Scanning Electron Microscopy) and were adjusted to yield a satisfactory fit in the UV/Vis part of the spectrum (tested values ranged from 1.1 to 1.82 Alexander et al., 2016; Kotrappa, 1971).

After these corrections, the resulting size distribution was fitted to a log-normal function to obtain the a priori values for the standard deviation σ, the total number of particle N ($particles.cm^{-3}$) and geometric radius r_g (μm).

3.2. Numerical approach

The numerical approach has been detailed in previous articles (Herbin et al., 2017; Hubert et al., 2017). A brief summary of the important points will be given in this section. First, the numerical procedure is fed by extinction spectra from IR to UV/visible spectral range and the size distribution recorded by the different devices specified in the previous section. These data consist of the main input parameters needed to launch the procedure. Then, the forward model used in this study is based on the work of Clarisse et al. (2010) and consist of making calculation of the extinction coefficient assuming the Mie theory to retrieve the imaginary part of the CRI. Then, the Kramers–Kronig(KK) relationships (Ahrenkiel, 1971) were applied to calculate the real component, as they link the real and the imaginary part of the CRI. However, the use of KK relationships, which is an equation with an infinite integral, requires inter- and extrapolation of the refractive index outside the measurement intervals (from 0 to 650 cm^{-1} and from 4000 to

10 000 cm^{-1}). Note that the fitting range was cut in four parts to give a strong weight where absorption bands were intense. In the IR, steps of 2 cm^{-1} were chosen from 650 to 1250 cm^{-1} because the intensity of the vibration band is maximal in this range. Then, steps were every 15 and 40 cm^{-1}, respectively from 1255 to 1840 cm^{-1} and from 1840 to 4000 cm^{-1}. In the UV spectral region, from 10 000 to 32 500 cm^{-1}, the resolution was set to 500 cm^{-1} because no significant absorption features are observed in this spectral range. The inverse model consists of an iterative optimal estimation method (OEM) of the imaginary component of the CRI. Then, the imaginary part of the CRI is adjusted at each iteration for each wavenumber to reduce the difference between the experimental extinction spectra and that simulated with Mie until reaching the convergence criterion.

To begin, the procedure requires an a priori state vector of retrieved parameters (x_a), which can be defined as the best knowledge that we have on the CRIs, especially the imaginary component κ.

In addition to a priori values, the optimal estimation retrieval also depends on constraints specified with covariance matrices. The a priori state vector is associated with a covariance matrix S_a which corresponds to the variability to the a priori values of n and κ. This covariance matrix was set to a constant diagonal value of 50% for n and κ because the a priori vector of n and κ remains the same for all the samples which require to leave a high variability for this parameter. Moreover, a noise diagonal matrix S_e has been built and was defined from the signal to noise ratio, where the noise was estimated from the difference between the smoothed and the observed extinction spectra. The signal to noise ratio in the IR was set to 300 and 100 in the UV/vis spectral region. The better signal/noise ratio in the IR spectral region is due to the use of a multi pass cell of optical length of 10 meters compare to a single pass cell in the UV/visible of 1 meter.

Moreover, an a priori state vector of non-retrieved parameters (x_b) is required and is defined as the best knowledge of the size distribution parameters. The three components of x_b are: the geometric standard deviation σ_g, the total number concentration of particles N (particles.cm^{-3}) and the mean geometric radius r_g (m), which are derived by fitting the experimental size distribution using a Log-normal law. Note that the experimental size distribution was not used directly to retrieve CRIs because it remains large uncertainties in the determination of the size and the concentration of poly-dispersed aerosols (Armendariz & Leith, 2002; Volckens & Peters, 2005). Nevertheless, the size distribution recorded by the APS was used as a first guess but after several adjustments. Indeed, it is well known that optical counters are less efficient in case of small particles (Peters & Leith, 2003; Volckens & Peters, 2005) that is why the concentration measured by the APS has been corrected using the empirical law mentioned in Thornburg, Cooper, and Leith (1999). After being corrected, the size distribution is fitted by a log-normal function and gives the a priori values of σ_g, N and r_g. As the size distribution remains the main source of uncertainty, this explains the fact that the covariance matrix of non-retrieved parameters (S_b) was built with a variability of 10% for the geometrical diameter, 20% for the concentration and 2% for the geometric standard deviation.

Finally, the last parameter to start the iterative process is the anchor point n_∞, which is required to apply the KK equation (Ahrenkiel, 1971; Lucarini, Saarinen, Peiponen, & Vartiainen, 2005) (see Eq. (2)).

$$n(\tilde{\nu}) - n_\infty = \frac{2}{\pi} P \int_0^\infty \frac{\tilde{\nu}' \kappa(\tilde{\nu}')}{\tilde{\nu}'^2 - \tilde{\nu}^2} d\tilde{\nu}' \tag{2}$$

With $\kappa(\tilde{\nu}')$ the imaginary part of the CRI at the specific wavenumber $\tilde{\nu}'$, $n(\tilde{\nu})$ the real part of the CRI at a specific wavenumber $\tilde{\nu}$ and P the Cauchy principal value. The anchor point can be determined using the UV-visible spectrum measured in laboratory exploiting the fact that the wavelength at which the maximum extinction occurs, is very sensitive to the value of the real part. Thus, we used the link between the real part of the CRI and the weight percent of SiO_2 to find an a priori value of the anchor point. For that, we referred to Prata et al. 2019 and Deguine et al.. 2020 which established a correlation between real part of the CRI and the weight percent of SiO_2. Then, the anchor point is automatically adjusted during the iterative procedure. The value of the anchor point has been accurately estimated for each samples as explained above, that is why the variability of the anchor point has been set to 1% to avoid non physical values.

At each iteration, the difference between the experimental spectra and the calculated spectra is automatically determined and a RMS (Root Mean Square) is calculated. the procedure ends when the convergence criteria is reached, which, in our case, means that the RMS is not decreasing any more.

4. Results and discussion

4.1. Extinction spectra

At the end of the iterative procedure presented in Section 3.2, the closest calculated extinction spectra compared to the experimental one is retained. The extinction spectra recorded and calculated at the end of the numerical procedure from the thermal infrared to the ultraviolet of the ten volcanic ash samples are presented in Fig. 2. Extinction Values has been cut at 3500 cm^{-1} due to the strong reduction of the efficiency of the detector.

The signal directly recorded by spectrometers can be noisy, especially in the UV-visible spectral region (Grey lines), which is why a smoothing has been performed using the Savitzky–Golay algorithm which is commonly use to smooth instrumental noise (Zhao, Tang, Zhang, & Liu, 2014). In the Infrared spectral region, a strong absorption feature can be observed between 800 and 1300 cm^{-1} for the ten different samples. These absorption bands are related to the vibration of T–O bonds [where T refers to fourfold coordinated cations (Si^{4+}, Al^{4+}, Fe^{3+}) and O non-bridging oxygen (NBO)]. As the major component of volcanic ash is amorphous silicate, the main absorption band centred around 1000 cm^{-1} is due to the asymmetric stretching vibrations of Si–O–Si bridges and the other one around 750 cm^{-1} is associated with symmetric vibrations of Si–O. There is not a strong difference in

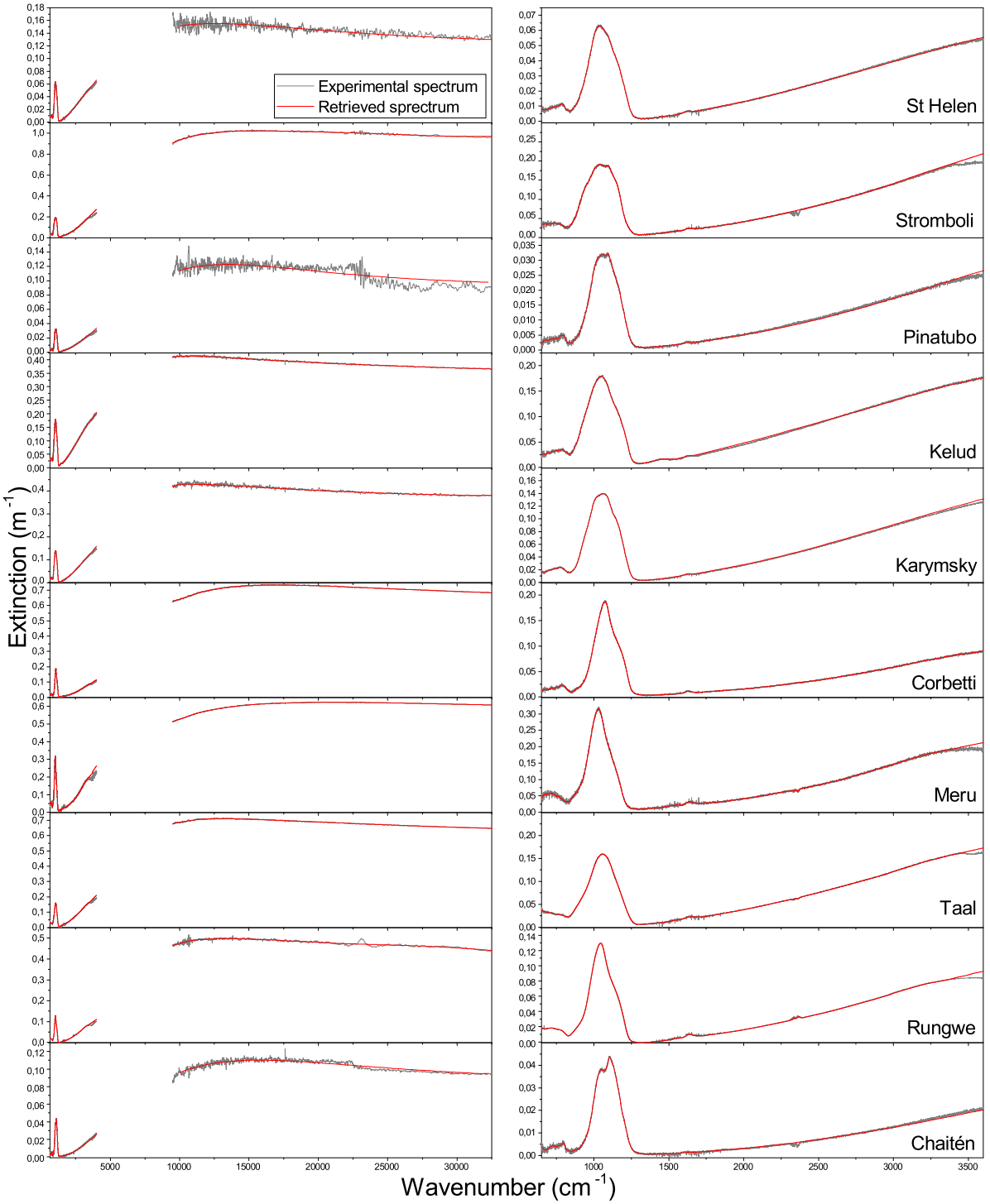

Fig. 2. Extinction spectra of volcanic ash samples. The left panels represents the full extinction in the IR and UV/visible spectral region and the right panels are a zoom in the IR. The grey and red lines correspond to the recorded extinction spectra and the simulated spectra obtained with the CRI derived at the end of the numerical procedure. (For interpretation of the references to colour in this figure legend, the reader is referred to the web version of this article.)

the shape of the absorption band around 750 cm^{-1} except for Stromboli, Rungwe and Taal where the feature looks flatter than in the other samples. Regarding the asymmetric stretching vibration band, most of samples show a broad absorption feature except for Corbetti, Meru and Rungwe where the peak is narrower and a small shoulder appeared around 1200 cm^{-1}. Moreover, the main

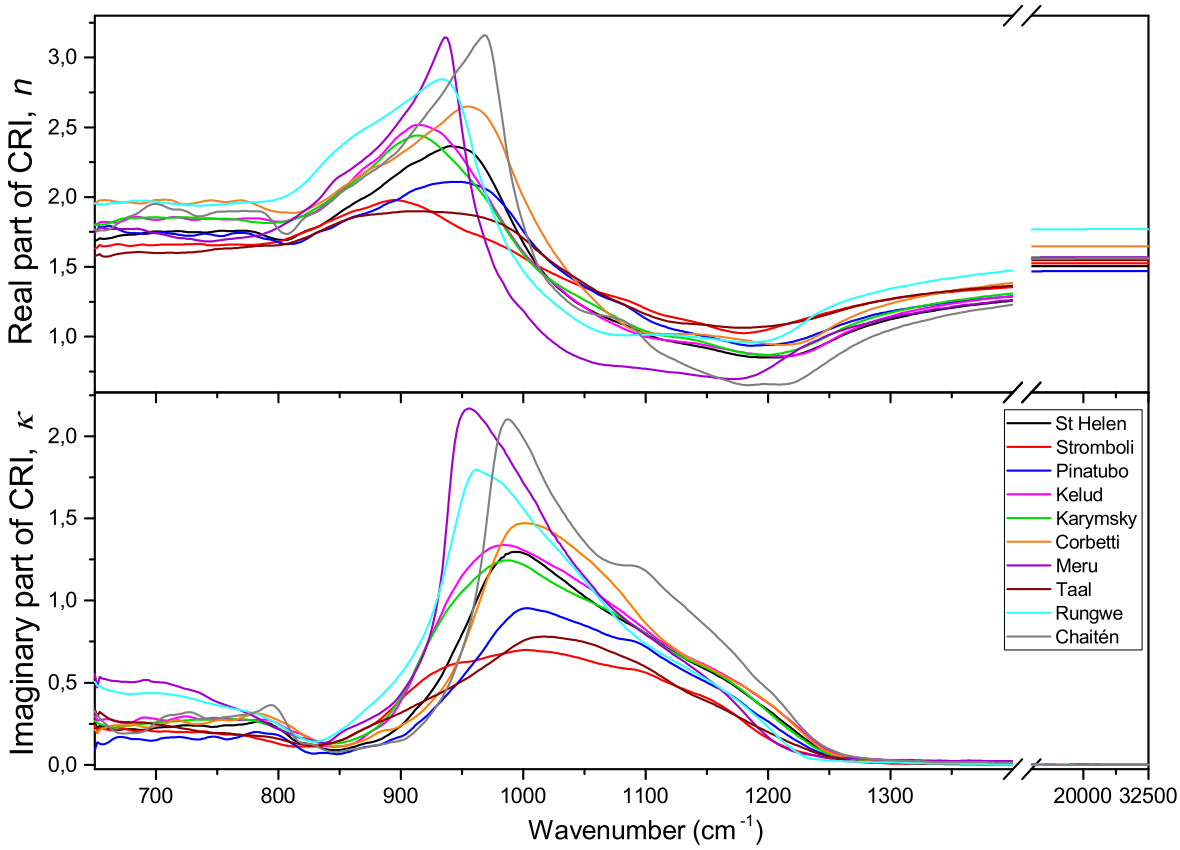

Fig. 3. Retrieved real and imaginary part of CRIs of the ten volcanic ash samples in Infrared and UV/visible spectral region.

absorption peak of Chaitén is split, possibly due to the high proportion of crystalline quartz in the sample and a high SiO_2 content (see Section 5.2). It has been already shown that increasing the SiO_2 content leads to a division of the single absorption peak and to a shift of the maximum toward higher wavenumber (Genova et al., 2015). The UV-visible part of the spectra does not show significant absorption features. The extinction is governed by the scattering, which dominates in this spectral region. However, we can note that the behaviour of the spectra can be slightly different from one sample to another. This is typically the case for the Kelud, Mount St. Helens and Karymsky samples which show a flatter dynamic than the other samples.

4.2. Complex refractive indices

The complex refractive indices of the ten volcanic ash samples retrieved using the algorithm detailed in Herbin et al. (2017) are presented in Fig. 3. The top and bottom panels respectively describe the behaviour of the real and imaginary part of the complex refractive index according to the wavenumber. For all samples, in the thermal infrared, the real part shows a big oscillation between 750 and 1300 cm^{-1} alternating with maximum and minimum values of n. In the UV-visible spectral region, the real and imaginary parts of the complex refractive index is almost constant. There is no strong absorption band in this region as highlighted by a value of the imaginary part of the CRI close to 0 in this spectral range. The position of the maximum and the minimum of the real part is shifted from one sample to another, with maxima located from 897 cm^{-1} for Stromboli to 968 cm^{-1} for Chaitén ash. The amplitude of these oscillations is also affected with a lowest value of 1.83 for Meru ash and a highest value of 3.15 for Chaitén ash. The imaginary part follows roughly the same behaviour than the real part with the maximum of the peak of Meru ash shifted to a lower wavenumber and situated at 911 cm^{-1} whereas it is shifted to a higher wavenumber for the Stromboli ash (1006 cm^{-1}). The amplitude of the imaginary part is also impacted by the nature of the ash with a minimum value of 0.70 obtained by Stromboli ash and a maximum value of 2.19 retrieved for Meru ash. The chemical composition of the ash clearly induces strong variations in the retrieved real and imaginary parts.

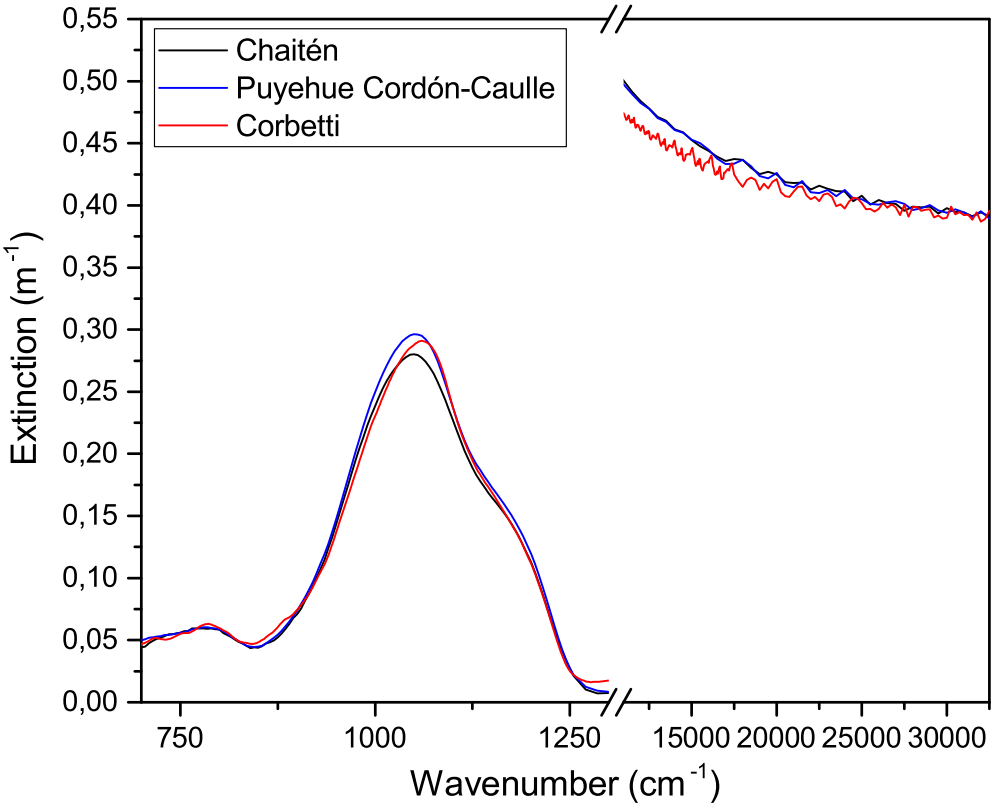

Fig. 4. Extinction spectra of four Rhyoitic volcanic ash samples: Chaitén, Chaitén2, Corbetti and Puyehue Cordón Caulle simulated with CRIs retrieved with Deguine et al. (2020) approach and the same size distribution.

5. Influence of the composition of the ash on CRIs

5.1. Oxide composition

The CRI's of ash particles depend on their chemical composition as pointed out by previous studies (e.g. Di Biagio et al., 2014; Prata et al., 2019). As the chemical nature of volcanic aerosols can be highly diverse, including due to the variability of erupted magma compositions at different volcanoes, it is important to obtain a representative set of CRIs that collectively correspond to a large amount of volcanoes on Earth. To do this, we compare the simulated extinction spectra of various volcanic ash samples which have a similar oxide composition. More precisely, we use three rhyolitic samples (see Fig. 1): Chaitén, Corbetti and Puyehue Cordón Caulle and we simulate the extinction spectra of each sample using the CRI and a unique size distribution. Fig. 4 shows the three simulated extinction spectra. The SiO_2 content of the samples varies from 69.5 to 74%. Their extinction spectra show the same behaviour in the UV/visible spectral region. The global shape and the amplitude of the vibrational band centred around 1000 cm^{-1} is similar for Corbetti, Chaitén and Puyehue Cordón Caulle with the unique band. The tiny differences in the behaviour of the extinction spectra could be explained by differences in the mineralogical compositions (see Section 5.2). Nevertheless, in view of the observations made through this comparison, it seems acceptable to use the refractive indices of chemically and mineralogically similar species if we do not specifically know their CRIs values. However, the use of non-specific indices to retrieve volcanic eruption plumes must be further investigated by trying to retrieve satellite measurements with non-specific indices but whose chemical and mineralogical composition is extremely close.

5.2. Crystalline/amorphous fraction

One of the parameters that can have an influence on the refractive index is the crystalline/amorphous fraction. Piontek, Hornby, Voigt, Bugliaro, and Gasteiger (2021) mentions the impact of the crystalline/amorphous fraction on the refractive indices. Fig. 5 shows the simulated extinction for 2 Chaitén samples but with a different crystalline/amorphous fraction using the unique size distribution mentioned in Section 5.1 and refractive indices determined in the previous study, Deguine et al. (2020) (Chaitén 88% amorphous) and from this study (Chaitén 34% amorphous). The black and red curves correspond to the extinction for a proportion of amorphous constituent of 34.5 and 88.1% respectively. Differences in crystalline/amorphous fraction between the two samples

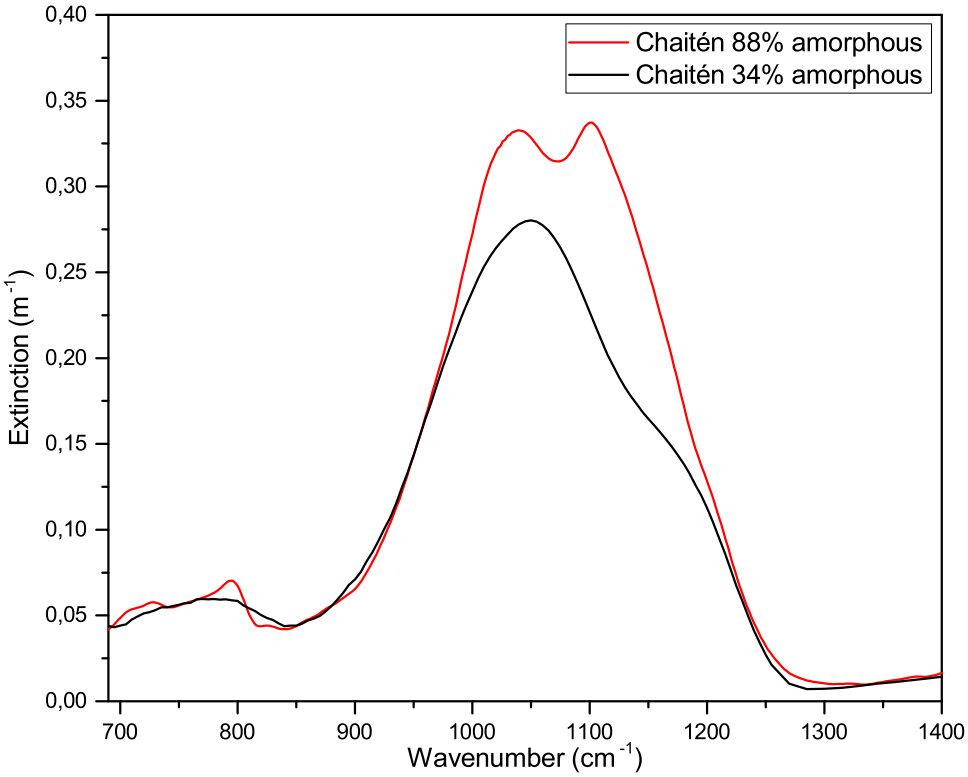

Fig. 5. Comparison of the extinction of Chaitén for different crystalline/amorphous fractions in the IR spectral window 690–1400 cm^{-1}. The red curve represents the extinction of Chaitén with a high amorphous content (≈88%) from Deguine et al. (2020). The black curve shows the extinction of an other Chaitén sample with a low amorphous fraction (≈34%). (For interpretation of the references to colour in this figure legend, the reader is referred to the web version of this article.)

could be explained by the nature of the samples. The one with the highest crystalline proportion comes from the dome collapse event of Chaitén in February 2009, which is almost one year after the eruption in May 2008 when we sampled the low crystalline one. A variation of the behaviour of the simulated extinction is notable depending on the proportion of amorphous species making up the sample. Indeed, between 700 and 850 cm^{-1} we can distinguish a double absorption band in the case of the less amorphous sample, which suggests a high content of crystalline silica, thus approaching the behaviour of quartz which has 2 absorption peaks in this wavenumber window (double peaks due to the expression of the ordinary and extraordinary part of the refractive index) (Peterson & Weinman, 1969). Conversely, when the content of amorphous compound increases, the shape of the refractive index is closer to that established for amorphous silica, with the presence of a single absorption peak in this wavenumber range. We can observe the same behaviour for the main peak located between 950 and 1200 cm^{-1} with, for the sample at 34% amorphous, the appearance of a shoulder which could correspond to the doubling of the absorption peak observed in the extinction spectra of crystalline quartz. It therefore seems essential to take into account the amorphous/crystalline fraction because the spectral behaviour of the refractive indices seems directly and strongly depends on this parameter. The contribution of new refractive indices according to the crystalline or amorphous nature of the components could help to fill the observation biases during the retrieval of the physical parameters of aerosols recorded via remote sensing instruments. This parameter has been little studied (Piontek et al., 2021) and could have a significant impact on optical properties of aerosols. It should be deeply investigated in future works and coupled with complementary XRD analysis of samples.

6. Conclusion

Complex refractive indices of ten volcanic ash samples have been retrieved from the thermal infrared to the ultraviolet spectral range using a recently proposed methodology and are available in supplementary materials (see Deguine, 2022). The strength of the retrieval is the association of experimental data such as the extinction spectra and the size distribution with a numerical approach using optimal estimation method and Mie theory. These CRIs of volcanic ash from various geographical locations and chemical compositions will be introduced in the existing databases (HITRAN, GEISA, ARIA) to better estimate the physical parameters (concentration, aerosol optical thickness, mass loading) of volcanic ash using ground-based and satellite remote sensing instruments. These results together with those from a previous paper (Deguine et al. (2020)) present a complete unique database of CRI covering all main parts of the TAS diagram, and importantly a large part of the ash-rich eruptions of the last 50 years (which therefore can

be considered representative of an important part of future eruptions). CRIs retrieval of a wide variety of volcanic ash samples from IR to UV/vis has never been done before and are long awaited by the remote sensing community. Moreover, a strong link between the mineralogical composition and the CRI, especially its crystalline/amorphous proportion, has been suggested and highlight the need to increase our knowledge on this parameter which has to be considered for the determination of the CRI to be used in remote sensing techniques.

Funding

The CaPPA project (Chemical and Physical Properties of the Atmosphere) is funded by the French National Research Agency (ANR) through the PIA (Programme d'Investissement d'Avenir) under contract "ANR-11-LABX-0 0 05-01" and by the Regional Council "Nord Pas de Calais-Picardie" and the "European Funds for Regional Economic Development" (FEDER). Part of this research was funded by the European Union's Horizon 2020 research programme for Societal challenges - smart, green and integrated transport under grant agreement no. 723986 as part of the EUNADICS-AV project.

Declaration of competing interest

The authors declare that they have no known competing financial interests or personal relationships that could have appeared to influence the work reported in this paper.

Data availability

Data will be made available on request.

Acknowledgements

The authors would like to thank M.P. Delplancke and T. Segato of the 4MAT - Ecole polytechnique of the Université libre de Bruxelles for the XRF analysis. L.C. is a research associate supported by the Belgian F.R.S-FNRS. The authors would also thank A. Bernard, P.F Coheur, G. Villarosa, V. Outes, I. Iskandar and P. Izbekov for providing the volcanic ash samples.

References

Ahrenkiel, R. K. (1971). Modified Kramers-Kronig analysis of optical spectra. *Journal of the Optical Society of America*, [ISSN: 0030-3941] *61*(12), 1651. http://dx.doi.org/10.1364/josa.61.001651.

Alexander, J. M., Bell, D. M., Imre, D., Kleiber, P. D., Grassian, V. H., & Zelenyuk, A. (2016). Measurement of size-dependent dynamic shape factors of quartz particles in two flow regimes. *Aerosol Science and Technology*, *50*(8), 870–879. http://dx.doi.org/10.1080/02786826.2016.1200006.

Ansmann, A., Tesche, M., Groß, S., Freudenthaler, V., Seifert, P., Hiebsch, A., et al. (2010). The 16 April 2010 major volcanic ash plume over central Europe: EARLINET lidar and AERONET photometer observations at Leipzig and Munich, Germany. *Geophysical Research Letters*, *37*(13), L13810. http://dx.doi.org/10.1029/2010gl043809.

Armendariz, A. J., & Leith, D. (2002). Concentration measurement and counting efficiency for the aerodynamic particle sizer 3320. *Journal of Aerosol Science*, *33*(1), 133–148. http://dx.doi.org/10.1016/s0021-8502(01)00152-5.

Bas, M. J. L., Maitre, R. W. L., Streckeisen, A., & Zanettin, B. (1986). A chemical classification of volcanic rocks based on the total alkali-silica diagram. *Journal of Petrology*, *27*(3), 745–750. http://dx.doi.org/10.1093/petrology/27.3.745.

Baxter, P. J., & Horwell, C. J. (2015). Impacts of eruptions on human health. In *The encyclopedia of volcanoes* (pp. 1035–1047). Elsevier, http://dx.doi.org/10.1016/b978-0-12-385938-9.00060-2.

Biagio, C. D., Boucher, H., Caquineau, S., Chevaillier, S., Cuesta, J., & Formenti, P. (2014). Variability of the infrared complex refractive index of african mineral dust: experimental estimation and implications for radiative transfer and satellite remote sensing. *Atmospheric Chemistry and Physics*, *14*(20), 11093–11116. http://dx.doi.org/10.5194/acp-14-11093-2014.

Cai, Y., Tay, K., Zheng, Z., Yang, W., Wang, H., Zeng, G., et al. (2018). Modeling of ash formation and deposition processes in coal and biomass fired boilers: A comprehensive review. *Applied Energy*, *230*, 1447–1544. http://dx.doi.org/10.1016/j.apenergy.2018.08.084.

Cao, Z., Bursik, M., Yang, Q., & Patra, A. (2021). Simulating the transport and dispersal of volcanic ash clouds with initial conditions created by a 3D plume model. *Frontiers in Earth Science*, *9*, http://dx.doi.org/10.3389/feart.2021.704797.

Carr, J. L., Horváth, Á., Wu, D. L., & Friberg, M. D. (2022). Stereo plume height and motion retrievals for the record-setting hunga Tonga-Hunga Ha'apai eruption of 15 January 2022. *Geophysical Research Letters*, *49*(9), http://dx.doi.org/10.1029/2022gl098131.

Casadevall, T. J., Delos Reyes, P., & Schneider, D. J. (1996). The 1991 pinatubo eruptions and their effects on aircraft operations. In C. Newhall, & R. Punongbayan (Eds.), *Fire and Mud: Eruptions and Lahars of Mount Pinatubo* (pp. 625–636). Philippines institute of volcanology and seismology/University of Washington Press, Quezon City/Seattle.

Clarisse, L., Hurtmans, D., Prata, A. J., Karagulian, F., Clerbaux, C., Mazière, M. D., et al. (2010). Retrieving radius, concentration, optical depth, and mass of different types of aerosols from high-resolution infrared nadir spectra. *Applied Optics*, *49*(19), 3713–3722. http://dx.doi.org/10.1364/AO.49.003713.

Dean, J., Taltavull, C., & Clyne, T. (2016). Influence of the composition and viscosity of volcanic ashes on their adhesion within gas turbine aeroengines. *Acta Materialia*, *109*, 8–16. http://dx.doi.org/10.1016/j.actamat.2016.02.011.

DeCarlo, P. F., Slowik, J. G., Worsnop, D. R., Davidovits, P., & Jimenez, J. L. (2004). Particle morphology and density characterization by combined mobility and aerodynamic diameter measurements. Part 1: Theory. *Aerosol Science and Technology*, *38*(12), 1185–1205. http://dx.doi.org/10.1080/027868290903907.

Deguine, A. (2022). Supplementary material figshare dataset. http://dx.doi.org/10.6084/M9.FIGSHARE.20037446.V1.

Deguine, A., Petitprez, D., Clarisse, L., Gudmundsson, S., Outes, V., Villarosa, G., et al. (2020). Complex refractive index of volcanic ash aerosol in the infrared, visible, and ultraviolet. *Applied Optics*, *59*(4), 884. http://dx.doi.org/10.1364/ao.59.000884.

Devi, P. S. R., Trupti, A. C., Nicy, A., Dalvi, A. A., Swain, K. K., Wagh, D. N., et al. (2015). Evaluation of uncertainty in the energy dispersive X-ray fluorescence determination of platinum in alumina. *Analytical Methods*, *7*(12), 5345–5351. http://dx.doi.org/10.1039/c5ay00547g.

Donovan, A., & Oppenheimer, C. (2010). The 2010 eyjafjallajökull eruption and the reconstruction of geography. *The Geographical Journal*, *177*(1), 4–11. http://dx.doi.org/10.1111/j.1475-4959.2010.00379.x.

Egan, W. G., Hilgeman, T., & Pang, K. (1975). Ultraviolet complex refractive index of martian dust: Laboratory measurements of terrestrial analogs. *Icarus*, *25*(2), 344–355. http://dx.doi.org/10.1016/0019-1035(75)90029-9.

Fontijn, K., Ernst, G. G., Elburg, M. A., Williamson, D., Abdallah, E., Kwelwa, S., et al. (2010). Holocene explosive eruptions in the Rungwe Volcanic Province, Tanzania. *Journal of Volcanology and Geothermal Research*, *196*(1–2), 91–110. http://dx.doi.org/10.1016/j.jvolgeores.2010.07.021.

Fontijn, K., McNamara, K., Tadesse, A. Z., Pyle, D. M., Dessalegn, F., Hutchison, W., et al. (2018). Contrasting styles of post-caldera volcanism along the Main Ethiopian Rift: Implications for contemporary volcanic hazards. *Journal of Volcanology and Geothermal Research*, *356*, 90–113. http://dx.doi.org/10.1016/j.jvolgeores.2018.02.001.

Genova, D. D., Morgavi, D., Hess, K.-U., Neuville, D. R., Borovkov, N., Perugini, D., et al. (2015). Approximate chemical analysis of volcanic glasses using Raman spectroscopy. *Journal of Raman Spectroscopy*, *46*(12), 1235–1244. http://dx.doi.org/10.1002/jrs.4751.

Gouhier, M., Eychenne, J., Azzaoui, N., Guillin, A., Deslandes, M., Poret, M., et al. (2019). Low efficiency of large volcanic eruptions in transporting very fine ash into the atmosphere. *Scientific Reports*, *9*, 1449. http://dx.doi.org/10.1038/s41598-019-38595-7.

Gudmundsson, M. T., Pedersen, R., Vogfjörd, K., Thorbjarnardóttir, B., Jakobsdóttir, S., & Roberts, M. J. (2010). Eruptions of Eyjafjallajökull Volcano, Iceland. *Transactions American Geophysical Union*, *91*(21), 190–191. http://dx.doi.org/10.1029/2010eo210002.

Guffanti, M., Casadevall, T. J., & Budding, K. (2010). Encounters of aircraft with volcanic ash clouds; a compilation of known incidents, 1953–2009. http://dx.doi.org/10.3133/ds545, U.S. Geological Survey Data Series 545, ver. 1.0, 12 p., plus 4 appendixes including the compilation database [https://pubs.usgs.gov/ds/545/].

Harvey, N. J., Huntley, N., Dacre, H. F., Goldstein, M., Thomson, D., & Webster, H. (2018). Multi-level emulation of a volcanic ash transport and dispersion model to quantify sensitivity to uncertain parameters. *Natural Hazards and Earth System Sciences*, *18*(1), 41–63. http://dx.doi.org/10.5194/nhess-18-41-2018.

Heffter, J. L., & Stunder, B. J. B. (1993). Volcanic ash forecast transport and dispersion (VAFTAD) model. *Weather and Forecasting*, *8*(4), 533–541. http://dx.doi.org/10.1175/1520-0434(1993)008<0533:VAFTAD>2.0.CO;2, URL https://journals.ametsoc.org/view/journals/wefo/8/4/1520-0434_1993_008_0533_vaftad_2_0_co_2.xml.

Herbin, H., Pujol, O., Hubert, P., & Petitprez, D. (2017). New approach for the determination of aerosol refractive indices – Part I: Theoretical bases and numerical methodology. *Journal of Quantitative Spectroscopy and Radiative Transfer*, *200*, 311–319. http://dx.doi.org/10.1016/j.jqsrt.2017.03.005.

Horwell, C. J., & Baxter, P. J. (2006). The respiratory health hazards of volcanic ash: a review for volcanic risk mitigation. *Bulletin of Volcanology*, *69*(1), 1–24. http://dx.doi.org/10.1007/s00445-006-0052-y.

Hubert, P., Herbin, H., Visez, N., Pujol, O., & Petitprez, D. (2017). New approach for the determination of aerosol refractive indices – Part II: Experimental set-up and application to amorphous silica particles. *Journal of Quantitative Spectroscopy and Radiative Transfer*, *200*, 320–327. http://dx.doi.org/10.1016/j.jqsrt.2017.03.037.

Kaminski, E., Tait, S., Ferrucci, F., Martet, M., Hirn, B., & Husson, P. (2011). Estimation of ash injection in the atmosphere by basaltic volcanic plumes: The case of the Eyjafjallajökull 2010 eruption. *Journal of Geophysical Research*, *116*, http://dx.doi.org/10.1029/2011jb008297.

Kisaka, M., Fontijn, K., Shemsanga, C., Tomašek, I., Gaduputi, S., Debaille, V., et al. (2021). The late Quaternary eruptive history of Meru volcano, northern Tanzania. *Journal of Volcanology and Geothermal Research*, *417*, Article 107314. http://dx.doi.org/10.1016/j.jvolgeores.2021.107314.

Kotrappa, P. (1971). Shape factors for quartz aerosol in respirable size range. *Journal of Aerosol Science*, *2*(3), 353–359. http://dx.doi.org/10.1016/0021-8502(71)90060-7.

Laakso, A., Kokkola, H., Partanen, A.-I., Niemeier, U., Timmreck, C., Lehtinen, K. E. J., et al. (2016). Radiative and climate impacts of a large volcanic eruption during stratospheric sulfur geoengineering. *Atmospheric Chemistry and Physics*, *16*(1), 305–323. http://dx.doi.org/10.5194/acp-16-305-2016.

Lombardo, D., Ciancio, N., Campisi, R., Maria, A. D., Bivona, L., Poletti, V., et al. (2013). A retrospective study on acute health effects due to volcanic ash exposure during the eruption of Mount Etna (Sicily) in 2002. *Multidisciplinary Respiratory Medicine*, *8*(1), 51. http://dx.doi.org/10.1186/2049-6958-8-51.

Lucarini, V., Saarinen, J. J., Peiponen, K.-E., & Vartiainen, E. M. (2005). *Kramers-Kronig relations in optical materials research, vol. 110*. Springer Science & Business Media.

de Michele, M., Raucoules, D., Corradini, S., Merucci, L., Salerno, G., Sellitto, P., et al. (2019). Volcanic cloud top height estimation using the plume elevation model procedure applied to orthorectified landsat 8 data. Test case: 26 October 2013 Mt. Etna Eruption. *Remote Sensing*, *11*(7), 785. http://dx.doi.org/10.3390/rs11070785.

Mosaffaei, Z., & Jahani, A. (2020). Modeling of ash (Fraxinus excelsior) bark thickness in urban forests using artificial neural network (ANN) and regression models. *Modeling Earth Systems and Environment*, *7*(3), 1443–1452. http://dx.doi.org/10.1007/s40808-020-00869-9.

Mueller, W., Cowie, H., Horwell, C. J., Hurley, F., & Baxter, P. J. (2020). Health impact assessment of volcanic ash inhalation: a comparison with outdoor air pollution methods. *Geo Health*, *4*(7), http://dx.doi.org/10.1029/2020gh000256.

Peters, T. M., & Leith, D. (2003). Concentration measurement and counting efficiency of the aerodynamic particle sizer 3321. *Journal of Aerosol Science*, *34*(5), 627–634. http://dx.doi.org/10.1016/s0021-8502(03)00030-2.

Peterson, R., Webley, P., D'Amours, R., Servranckx, R., Stunder, B., & Papp, K. (2015). Volcanic ash transport and dispersion models. In *Monitoring volcanoes in the north pacific* (pp. 187–233). Springer Berlin Heidelberg, http://dx.doi.org/10.1007/978-3-540-68750-4_7.

Peterson, J. T., & Weinman, J. A. (1969). Optical properties of quartz dust particles at infrared wavelengths. *Journal of Geophysical Research*, *74*(28), 6947–6952. http://dx.doi.org/10.1029/jc074i028p06947.

Piontek, D., Hornby, A., Voigt, C., Bugliaro, L., & Gasteiger, J. (2021). Determination of complex refractive indices and optical properties of volcanic ashes in the thermal infrared based on generic petrological compositions. *Journal of Volcanology and Geothermal Research*, *411*, Article 107174. http://dx.doi.org/10.1016/j.jvolgeores.2021.107174.

Plu, M., Bigeard, G., Sič, B., Emili, E., Bugliaro, L., Amraoui, L. E., et al. (2021). Modelling the volcanic ash plume from Eyjafjallajökull eruption (May 2010) over Europe: evaluation of the benefit of source term improvements and of the assimilation of aerosol measurements. *Natural Hazards and Earth System Sciences*, *21*(12), 3731–3747. http://dx.doi.org/10.5194/nhess-21-3731-2021.

Pollack, J. B., Toon, O. B., & Khare, B. N. (1973). Optical properties of some terrestrial rocks and glasses. *Icarus*, *19*(3), 372–389. http://dx.doi.org/10.1016/0019-1035(73)90115-2.

Prata, G. S., Ventress, L. J., Carboni, E., Mather, T. A., Grainger, R. G., & Pyle, D. M. (2019). A new parameterization of volcanic ash complex refractive index based on NBO/T and SiO_2 content. *Journal of Geophysical Research*, *124*(3), 1779–1797. http://dx.doi.org/10.1029/2018jd028679.

Railsback, L. B. (2006). Some fundamentals of mineralogy and geochemistry. In *On-Line Book*. Quoted from: Www. Gly. Uga. Edu/Railsback.

Reed, B. E., Peters, D. M., McPheat, R., & Grainger, R. G. (2018). The complex refractive index of volcanic ash aerosol retrieved from spectral mass extinction. *Journal of Geophysical Research*, *123*(2), 1339–1350. http://dx.doi.org/10.1002/2017jd027362.

Reyes, P. J. D., Bornas, M. A. V., Dominey-Howes, D., Pidlaoan, A. C., Magill, C. R., & Renato U. Solidum, J. (2018). A synthesis and review of historical eruptions at Taal Volcano, Southern Luzon, Philippines. *Earth-Science Reviews*, *177*, 565–588. http://dx.doi.org/10.1016/j.earscirev.2017.11.014.

Rossi, E., Bagheri, G., Beckett, F., & Bonadonna, C. (2021). The fate of volcanic ash: premature or delayed sedimentation? *Nature Communications*, *12*(1), http://dx.doi.org/10.1038/s41467-021-21568-8.

Shinozaki, M., Roberts, K. A., van de Goor, B., & Clyne, T. W. (2013). Deposition of ingested volcanic ash on surfaces in the turbine of a small jet engine. *Advanced Engineering Materials*, 986–994. http://dx.doi.org/10.1002/adem.201200357.

Sigmundsson, F., & Höskuldsson, Á. (2010). Develop instruments to monitor volcanic ash fallout. *Nature*, *466*(7302), 28. http://dx.doi.org/10.1038/466028b.

Stohl, A., Prata, A. J., Eckhardt, S., Clarisse, L., Durant, A., Henne, S., et al. (2011). Determination of time and height resolved volcanic ash emissions and their use for quantitative ash dispersion modeling: the 2010 eyjafjallajökull eruption. *Atmospheric Chemistry and Physics*, *11*(9), 4333–4351. http://dx.doi.org/10.5194/acp-11-4333-2011.

Thompson, M. A., Lindsay, J. M., Wilson, T. M., Biass, S., & Sandri, L. (2016). Quantifying risk to agriculture from volcanic ashfall: a case study from the Bay of Plenty, New Zealand. *Natural Hazards*, *86*(1), 31–56. http://dx.doi.org/10.1007/s11069-016-2672-7.

Thornburg, J., Cooper, S. J., & Leith, D. (1999). Counting efficiency of the API aerosizer. *Journal of Aerosol Science*, *30*(4), 479–488. http://dx.doi.org/10.1016/s0021-8502(98)00073-1.

Tomašek, I., Damby, D. E., Andronico, D., Baxter, P. J., Boonen, I., Claeys, P., et al. (2021). Assessing the biological reactivity of organic compounds on volcanic ash: implications for human health hazard. *Bulletin of Volcanology*, *83*(5), http://dx.doi.org/10.1007/s00445-021-01453-4.

Vernier, J.-P., Fairlie, T. D., Deshler, T., Natarajan, M., Knepp, T., Foster, K., et al. (2016). In situ and space-based observations of the Kelud volcanic plume: The persistence of ash in the lower stratosphere. *Journal of Geophysical Research: Atmospheres*, *121*(18), http://dx.doi.org/10.1002/2016jd025344.

Volckens, J., & Peters, T. M. (2005). Counting and particle transmission efficiency of the aerodynamic particle sizer. *Journal of Aerosol Science*, *36*(12), 1400–1408. http://dx.doi.org/10.1016/j.jaerosci.2005.03.009.

Volz, F. E. (1973). Infrared optical constants of ammonium sulfate, sahara dust, volcanic pumice, and flyash. *Applied Optics*, *12*(3), 564–568. http://dx.doi.org/10.1364/ao.12.000564.

Wilson, T. M., & Cole, J. W. (2007). Potential impact of ash eruptions on dairy farms from a study of the effects on a farm in eastern Bay of Plenty, New Zealand implications for hazard mitigation. *Natural Hazards*, *43*(1), 103–128. http://dx.doi.org/10.1007/s11069-007-9111-8.

Wilson, T. M., Stewart, C., Sword-Daniels, V., Leonard, G. S., Johnston, D. M., Cole, J. W., et al. (2012). Volcanic ash impacts on critical infrastructure. *Physics and Chemistry of the Earth, Parts A/B/C*, *45–46*, 5–23. http://dx.doi.org/10.1016/j.pce.2011.06.006.

Zhao, A.-X., Tang, X.-J., Zhang, Z.-H., & Liu, J.-H. (2014). The parameters optimization selection of Savitzky-Golay filter and its application in smoothing pretreatment for FTIR spectra. In *2014 9th IEEE Conference on industrial electronics and applications*. IEEE, http://dx.doi.org/10.1109/iciea.2014.6931218.

Zhu, Y., Toon, O. B., Jensen, E. J., Bardeen, C. G., Mills, M. J., Tolbert, M. A., et al. (2020). Persisting volcanic ash particles impact stratospheric SO2 lifetime and aerosol optical properties. *Nature Communications*, *11*(1), http://dx.doi.org/10.1038/s41467-020-18352-5.